



ELSEVIER

Available online at www.sciencedirect.com**ScienceDirect**

Acta Materialia 91 (2015) 304–317

www.elsevier.com/locate/actamat

The role of low-lying optical phonons in lattice thermal conductance of rare-earth pyrochlores: A first-principle study

Guoqiang Lan, Bin Ouyang and Jun Song*

Department of Mining and Materials Engineering, McGill University, Montreal, Quebec H3A 0C5, Canada

Received 29 January 2015; revised 23 February 2015; accepted 1 March 2015

Available online 2 April 2015

Abstract—Rare-earth pyrochlores, commonly exhibiting remarkably low lattice thermal conductivities, are considered as promising topcoat materials for thermal barrier coatings. However the structural origin underlying their low thermal conductivities remains unclear. In the present study, we investigated the phonon properties of two groups of RE pyrochlores, $\text{Ln}_2\text{Zr}_2\text{O}_7$ ($\text{Ln} = \text{La}, \text{Nd}, \text{Sm}, \text{Gd}$) and $\text{Gd}_2\text{T}_2\text{O}_7$ ($\text{T} = \text{Zr}, \text{Hf}, \text{Sn}, \text{Pb}$) employing density functional theory and quasi harmonic approximation. Through the relaxation time approximation (RTA) with Debye model, the thermal conductivities of those RE pyrochlores were predicted, showing good agreement with experimental measurements. The low thermal conductivities of RE pyrochlores were shown to largely come from the interference between the low-lying optical branches and acoustic branches. The structural origin underlying the low-lying optical branches was then clarified and the competition between scattering processes in transverse and longitude acoustic branches was discussed.

© 2015 Acta Materialia Inc. Published by Elsevier Ltd. All rights reserved.

Keywords: Rare-earth; Pyrochlores; Phonon dispersion; Thermal conductivity; Density functional theory

1. Introduction

Thermal barrier coating (TBC) [1–3] is an essential constituent in gas turbine engines. It is applied to surfaces of superalloy components in the engine, shielding them from the hot gas to allow an operating temperature much higher than their melting temperatures. The thermal insulation from TBC is determined by the outmost ceramic topcoat [1–3]. Currently the common material used for the top coat is 7 wt.% yttria stabilized zirconia (7YSZ) because of its relatively low thermal conductivity ($2.0\text{--}3.0 \text{ W m}^{-1} \text{ K}^{-1}$) [4,5], good toughness [6,7] and thermochemical compatibility with the underlying TGO [4,8]. However, 7YSZ suffers from accelerated sintering kinetics [9,10] and destabilization of the desirable metastable t' phase at elevated temperatures [11], and susceptibility to calcium-magnesium aluminosilicate (CMAS) penetration [12,13], which significantly degrades its insulating efficiency, strain tolerance and intrinsic toughness, being greatly detrimental to its performance and durability. These limitations necessitate innovation to develop alternative coating materials.

Rare-earth (RE) pyrochlores recently emerge as potential candidate materials for the next-generation top coat given their low intrinsic thermal conductivities (i.e., $1\text{--}2 \text{ W m}^{-1} \text{ K}^{-1}$) [14–19]. The RE pyrochlore also exhibits high

temperature stability [4], similar thermal expansion coefficient as its beneath substrate [20,21], and can react with the CMAS melt to seal the surface against further infiltration [22]. In addition, RE pyrochlores can well preserve the pore content and architecture owing to their sluggish sintering kinetics [23]. The thermal properties of various RE pyrochlores were well characterized in many experimental studies [14–19]. It was postulated in some studies [24,25] that the abnormally low thermal conductivities of these pyrochlores may be attributed to the abundance of intrinsic oxygen vacancies and low-lying optical phonons due to RE element rattling. However the exact structural origin and phonon characteristics, particularly at the atomic level, remain largely unknown. Recently a few studies attempted to model and understand the thermal transport in pyrochlores. Liu et al. [26] and Feng et al. [27,28] investigated the thermal conductivities of $\text{Ln}_2\text{Zr}_2\text{O}_7$, $\text{Ln}_2\text{Sn}_2\text{O}_7$ ($\text{Ln} = \text{La}, \text{Nd}, \text{Sm}, \text{Gd}$) and $\text{La}_2\text{T}_2\text{O}_7$ ($\text{T} = \text{Ge}, \text{Ti}, \text{Sn}, \text{Zr}, \text{Hf}$) systems using density functional theory (DFT). In their studies, several physical properties, including elastic constants, lattice spacing and density, were computed from first-principles calculations, and subsequently combined with the simple formulas suggested by Clarke [29], Slack [30] and Cahill et al. [31] to estimate the minimum thermal conductivity. The estimated values yield good ball-park agreements with experimental measurements. Nonetheless, those studies fail to distinguish different RE pyrochlores in terms of thermal conductivity and thus do not reveal the mechanistic origin of lattice heat conduction.

* Corresponding author; e-mail: jun.song2@mcgill.ca

In this paper, we employ the approach of relaxation-time approximation (RTA) together with the Debye model [32] to study the high-temperature thermal conductivities of several RE pyrochlores. Different from the simple models invoked in those previous modeling studies of pyrochlore oxides [26–28,33], this approach allows direct considerations of phonon scattering processes and anharmonic relaxation times, and is evidenced by a few studies to an accurate method to predict the thermal conductivity for a wide variety of solid-state materials [32,34–36]. We focused on two sets of RE pyrochlores, $\text{Ln}_2\text{Zr}_2\text{O}_7$ ($\text{Ln} = \text{La}, \text{Nd}, \text{Sm}, \text{Gd}$) and $\text{Gd}_2\text{T}_2\text{O}_7$ ($\text{T} = \text{Zr}, \text{Hf}, \text{Sn}, \text{Pb}$). Through first-principle DFT calculations, the ground-state crystal structures and corresponding elastic constants of those pyrochlores were obtained. Meanwhile the harmonic and anharmonic vibrational properties, including phonon density of states (DOS), phonon dispersion and Grüneisen parameters, are thoroughly investigated by DFT phonon calculations within the quasi harmonic approximation (QHA) [37]. Using the information obtained from DFT, the thermal conductivities of the RE pyrochlores considered were evaluated within RTA along with the Debye approximation, and compared with the ones estimated from Clarke's and Cahill's models. The predictions from RTA along with the Debye approximation were demonstrated to effectively differentiate between different RE pyrochlores and yield much more consistent agreement with experimental data. Finally, the atomic vibration patterns contributing to the low-lying optical modes that scatter the acoustic modes were investigated to clarify the mechanistic origin of the low thermal conductivity of RE pyrochlores.

2. Methodology

2.1. Density functional theory and phonon calculations

DFT calculations were performed using the Vienna ab initio simulation package (VASP) [39,40] with Perdew–Burke–Ernzerhof GGA approach [41] based on plane-wave basis sets. Valence configurations of the elements used in this study are as follows: La- $5s^2 5p^6 5d^1 6s^2$, Nd- $5s^2 5p^6 4f^1 6s^2$ ($4f^3$ frozen in the core), Sm- $5s^2 5p^6 4f^1 6s^2$ ($4f^5$ frozen in the core), Gd- $4f^7 5s^2 5p^6 5d^1 6s^2$, Zr- $4s^2 4p^6 5d^2 5s^2$, Hf- $5s^2 5p^6 5d^2 6s^2$, Sn- $5s^2 5p^2$, Pb- $6s^2 6p^2$, and O- $2s^2 2p^4$. The values of the Hubbard energy U [42,43] for Gd $4f$ valence electrons were set following Ref. [27]. The electron–core interaction was described by the Blöchl's projector augmented wave method (PAW) within the frozen-core approximation [44]. For the structural optimization and computation of elastic constants, a conventional pyrochlore cubic unit cell containing 88 atoms was constructed, and a $2 \times 2 \times 2$ Monkhorst–Pack (MP) k -mesh for Brillouin-zone integrations and a cutoff energy of 450 eV for the plane-wave basis set were used in the DFT calculations with convergence criteria for energy and force on each ion set as 10^{-9} eV and 10^{-6} eV Å $^{-1}$, respectively. The real-space force constants were obtained with the density-functional perturbation theory (DFPT) [45] using $2 \times 2 \times 2$ supercells (176 atoms) constructed from the pyrochlore primitive cell (22 atoms). The phonon properties were evaluated using PHONOPY [46] on $23 \times 23 \times 23$ q grid for all the RE pyrochlore systems. In the phonon calculations within QHA, the cell volume was varied by $\pm 0.75\%$ with respect to the equilibrium volume.

2.2. Models for lattice thermal conductivity

2.2.1. Minimum thermal conductivity based on Clarke's and Cahill's model

The concept of minimum thermal conductivity, κ_{\min} , was developed by Slack [47], stating that for a material there is a lower limit for the intrinsic thermal conductivity. It is of great technological importance to the TBC material research and has been widely used to predict the plateau thermal conductivities of poly-ion ceramic oxides at high temperature. Clarke et al. [29] proposed an expression of κ_{\min} , assuming that the phonon mean free path is identical to the inter-atomic spacing and the specific heat approaches $3k_B$ (k_B being the Boltzmann's constant) per atom above the Debye temperature:

$$\kappa_{\min} = 0.87k_B \bar{M}^{-2/3} E^{1/2} \rho^{1/6}, \quad (1)$$

where \bar{M} is the average mass of per atom, E is Young's modulus and ρ is the density. In the work by Cahill et al. [31], in accordance with Einstein's notion of lattice vibration, they assume that individual oscillators vibrate independently of one another and the phonon scattering time is one half the period of vibration. Under those assumptions, κ_{\min} at high temperature limit can be expressed as

$$\kappa_{\min} = \frac{k_B}{2.48} p^{2/3} (v_l + 2v_t) \quad (2)$$

where p is the density of number of atoms per volume, and v_l and v_t are the average longitudinal and transverse sound velocities respectively. As apparently illustrated in Eqs. (1) and (2), both Clarke's and Cahill's models predict that lower κ_{\min} requires smaller modulus (or sound velocity) and larger size of the unit cell.

2.2.2. Relaxation-time approximation (RTA) with the Debye model

RTA is commonly invoked in the treatment of Boltzmann transport equation (BTE) [32]. Given that it is usually difficult to consider various phonon scattering relaxation times for the full phonon dispersions, RTA is often augmented by the Debye model to simplify the phonon branches.

Phonon dispersion curves normally consist of low-frequency acoustic and high-frequency optical branches [32]. Generally, only acoustic phonons are effective for heat conduction, whereas optical phonons contribute very little to heat transport [32]. Consequently the total thermal conductivity, κ can be simplified as just a sum of contributions from two transverse (κ_{TA} and $\kappa_{TA'}$) and one longitudinal (κ_{LA}) acoustic phonon branches as discussed in Refs [34–36]:

$$\kappa = \kappa_{TA} + \kappa_{TA'} + \kappa_{LA}. \quad (3)$$

These partial conductivities κ_i ($i = TA, TA'$ or LA stands for two transverse and one longitudinal acoustic phonon branches, respectively) are given by RTA with Debye approximation [32] as:

$$\kappa_i = \frac{k_B}{2\pi^2 v_i} \left(\frac{k_B T}{\hbar} \right)^3 \int_0^{\tilde{\Theta}_i/T} \tau_q \frac{x^4 e^x}{(e^x - 1)^2} dx \quad (4)$$

where \hbar is the reduced Plank constant, T is temperature, v_i is corresponding acoustic phonon velocity, and $x = \hbar\omega/k_B T$ is a dimensionless quantity with ω being the phonon frequency. $\tilde{\Theta}_i$ is the reduced Debye temperature determined from the conventional Debye temperature, Θ_i , given in

Eq. (5) below for a crystal with n atoms per unit cell and the atomic volume being a^3 [48–50]

$$\tilde{\Theta}_i = \Theta_i n^{-1/3} \quad (5)$$

$$\Theta_i = \frac{\hbar}{k_B} \left(\frac{6\pi^2}{a^3} \right)^{1/3} v_i \quad (6)$$

The parameter τ_q represents the total scattering time due to various resistive processes, Umklapp scattering (U), phonon-point-defect scattering (PD), phonon-boundary scattering (B) etc. [32]. In perfect insulators at high temperatures, U-processes dominate the phonon scattering process, and thus we have $\tau_q^{-1} \approx \tau_U^{-1}$. Based on the Leibfried and Schlomann model [51], Slack et al. [52] suggested the following form for Umklapp scattering rate:

$$\frac{1}{\tau_U^i(x)} \approx \frac{\hbar \bar{\gamma}_i^2}{M v_i^2 \tilde{\Theta}_i} \left(\frac{k_B}{\hbar} \right)^2 x^2 T^3 \exp(-\tilde{\Theta}_i/3T) \quad (7)$$

where $\bar{\gamma}_i$ is the average Grüneisen parameter for the i ($i = \text{TA}, \text{TA}'$ or LA) acoustic branch and M is the average mass per atom in the material. Other formulas of the Umklapp scattering rate also exist, all showing τ_U^{-1} proportional to γ^2 [48,53,54]. The mode Grüneisen parameter can be obtained as [32,55]

$$\gamma(q, s) = -\frac{V}{\omega(q, s)} \frac{\partial \omega(q, s)}{\partial V}, \quad (8)$$

where $\gamma(q, s)$ and $\omega(q, s)$ represent the mode Grüneisen parameter and phonon frequency at wave vector q and branch s . $\gamma(q, s)$ can be interpreted as the rate of change of $\omega(q, s)$ with unit cell volume V . The average Grüneisen parameter $\bar{\gamma}$ for each acoustic branch can be obtained as

$$\bar{\gamma} = \frac{\sum_{q,s} |\gamma(q, s)| C(q, s)}{\sum_{q,s} C(q, s)}, \quad (9)$$

where $C(q, s)$ is mode specific heat capacity at wave vector q and branch s , and the absolute value of mode Grüneisen

parameter $|\gamma(q, s)|$ is used to avoid cancellation between different modes. All the parameters in the above equations can be obtained directly from first-principle DFT calculations, allowing the estimation of the thermal conductivity without any empirical data inputs. In the context below, RTA with the Debye model is shortened as RTA model for simplicity.

3. Results and discussion

3.1. Structural parameters and elastic constants

The crystal structure for the RE pyrochlore oxides is illustrated in Fig. 1, where the relative positions of cations (i.e., Ln^{3+} and T^{4+}) and anions (i.e., O^{2-} and O'^{2-}) are indicated. The corresponding lattice constants and 48/ f position parameters (i.e., x) are optimized via DFT calculations, listed in Table 1 where the values from experiments [21,56–60] are also listed for comparison. We note that for all materials considered the theoretical value deviates from the experimental one by less than 1%.

Table 2 lists the values of anisotropic elastic constants and moduli (Voigt averages [62]) obtained from DFT calculations, and the corresponding experimental data available in literature [63–65]. Despite some absence of experimental data, overall we note that the theoretical values are in good agreement with experimental measurements. In particular for $\text{Ln}_2\text{Zr}_2\text{O}_7$, it is worth noting that our present results exhibit better agreement with experimental data than the ones results calculated using LSDA + U [27]. The good agreement between our DFT predictions and experimental data (cf. Tables 1 and 2) confirms the GGA + U method is suitable for calculations of the RE pyrochlore systems.

Comparing those parameters in Table 2 among different pyrochlores, we note that they do not show an apparent relationship with the radii of Ln^{3+} or T^{4+} cations. Particularly concerning the calculated values, we see that

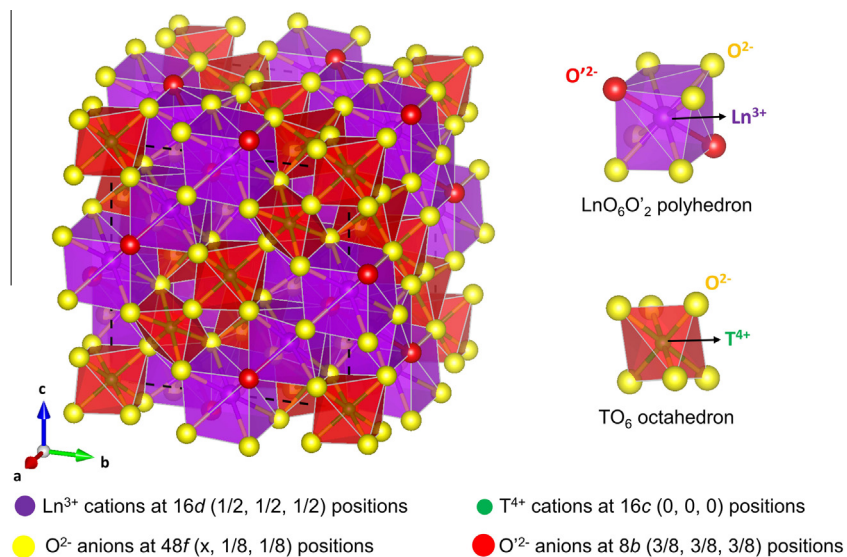


Fig. 1. Crystal structure of $\text{Ln}_2\text{T}_2\text{O}_7$ type pyrochlore (with the space group being $Fm\bar{3}m$ and a chemical formula as $\text{Ln}_2\text{T}_2\text{O}_6\text{O}'$). The structure are occupied by four crystallographically unique atomic sites [38]: larger Ln^{3+} cations at $16d$, smaller T^{4+} cations at $16c$, O^{2-} anions at $48f$ and O'^{2-} anions at $8b$. Parameter x is used to represent the off-center property of O anion at $48f$ position. The two polyhedral, i.e., $\text{LnO}_6\text{O}'_2$ and TO_6 , that compose the pyrochlore are illustrated by the two subfigures on the right.

Table 1. Calculated and experimental values of the lattice constant, a (Å) and 48f position parameter x for $\text{Ln}_2\text{Zr}_2\text{O}_7$ ($\text{Ln} = \text{La}, \text{Nd}, \text{Sm}$ and Gd) and $\text{Gd}_2\text{T}_2\text{O}_7$ ($\text{T} = \text{Pb}, \text{Zr}, \text{Hf}$ and Sn). The parameter r_{Ln}/r (pm) denotes the corresponding $\text{Ln}^{3+}/\text{T}^{4+}$ cation radius [61].

$r_{\text{Ln}}/r_{\text{T}}$	$\text{La}_2\text{Zr}_2\text{O}_7$		$\text{Nd}_2\text{Zr}_2\text{O}_7$		$\text{Sm}_2\text{Zr}_2\text{O}_7$		$\text{Gd}_2\text{Zr}_2\text{O}_7$		$\text{Gd}_2\text{Hf}_2\text{O}_7$		$\text{Gd}_2\text{Pb}_2\text{O}_7$		$\text{Gd}_2\text{Sn}_2\text{O}_7$	
	Cal. ^a	Exp. ^b	Cal. ^a	Exp. ^c	Cal. ^a	Exp. ^d	Cal. ^a	Exp. ^e	Cal. ^a	Exp. ^f	Cal. ^a	Exp. ^g	Cal. ^a	Exp. ^h
a	10.83	10.78	10.74	10.67	10.66	10.58	10.60	10.53	10.55	10.49	10.83	10.72	10.54	10.45
x	0.332	0.332	0.335	0.335	0.337	0.339	0.338	0.340	0.337	0.348	0.348	0.338	0.338	0.335

^a This work (GGA + U).^b Ref. [56].^c Ref. [57].^d Ref. [58].^e Ref. [57].^f Ref. [21].^g Ref. [59].^h Ref. [60].**Table 2.** Calculated and experimental values of anisotropic elastic constants (in GPa), i.e., C_{11} , C_{12} , C_{44} , bulk modulus B (GPa), shear modulus G (GPa), Yong's modulus E (GPa), the Poisson's ratio v , and the B/G ratio. The parameter r_{Ln}/r (pm) denotes the corresponding $\text{Ln}^{3+}/\text{T}^{4+}$ cation radius.

$r_{\text{Ln}}/r^{\text{e}}$	Method	C_{11}	C_{44}	C_{12}	B	E	G	v	B/G	
$\text{La}_2\text{Zr}_2\text{O}_7$	103.2/72.0	Cal. ^a Exp. ^b	266 239	87 107	110 162	162 224	213 88	83 0.273	1.95 1.87	
$\text{Nd}_2\text{Zr}_2\text{O}_7$	98.3/72.0	Cal. ^a Exp. ^c	279 219	89 86	107 164	164 226	224 89	86 0.271	1.88	
$\text{Sm}_2\text{Zr}_2\text{O}_7$	95.8/72.0	Cal. ^a Exp. ^c	286 231	88 90	107 167	167 226	226 89	0.274 0.277	1.88	
$\text{Gd}_2\text{Zr}_2\text{O}_7$	93.5/72.0	Cal. ^a Exp. ^c Exp. ^d	289 156 175	85 205 238	103 165 175	165 224 89	224 88 89	0.273 0.276 0.283	1.87 1.95 1.97	
$\text{Gd}_2\text{Hf}_2\text{O}_7$	93.5/71.0	Cal. ^a	301	94	105	170	242	96	0.264	1.78
$\text{Gd}_2\text{Pb}_2\text{O}_7$	93.5/77.5	Cal. ^a	248	67	93	145	183	71	0.289	2.03
$\text{Gd}_2\text{Sn}_2\text{O}_7$	93.5/69.0	Cal. ^a	289	87	107	168	226	89	0.275	1.89

^a This work.^b Ref. [63].^c Ref. [64].^d Ref. [65].^e Ref. [61].

for the $\text{Ln}_2\text{Zr}_2\text{O}_7$ group, the moduli of $\text{La}_2\text{Zr}_2\text{O}_7$ are the lowest, while those of other pyrochlores (i.e., $\text{Ln} = \text{Nd}, \text{Sm}, \text{Gd}$) are almost the same. For the $\text{Gd}_2\text{T}_2\text{O}_7$ group, $\text{Gd}_2\text{Pb}_2\text{O}_7$ and $\text{Gd}_2\text{Hf}_2\text{O}_7$ exhibit lowest and highest moduli respectively, while $\text{Gd}_2\text{Zr}_2\text{O}_7$ and $\text{Gd}_2\text{Sn}_2\text{O}_7$ have similar moduli.

3.2. Phonon dispersion and vibrational properties

3.2.1. Phonon dispersion curves and partial density of states

The calculated phonon dispersion curves along high-symmetry directions in their Brillouin zones (BZ) and partial density of states (PDOS) for $\text{Ln}_2\text{Zr}_2\text{O}_7$ ($\text{Ln} = \text{La}, \text{Nd}, \text{Sm}, \text{Gd}$) and $\text{Gd}_2\text{T}_2\text{O}_7$ ($\text{T} = \text{Zr}, \text{Hf}, \text{Sn}, \text{Pb}$) are shown in Figs. 2 and 3 respectively. In all the plots shown in Figs. 2 and 3, we see there are low-lying optical branches (between 1 and 3 THz) lying in the acoustic range. The low-lying optical branches are identified to be primarily attributed to the vibrations of Ln^{3+} cations.

From Fig. 2, we see that the shapes of the phonon dispersions curves and PDOS of the $\text{Ln}_2\text{Zr}_2\text{O}_7$ pyrochlores are in general rather similar. However we can note that

for $\text{La}_2\text{Zr}_2\text{O}_7$, the optical branches attributed to Ln^{3+} cation are higher while the high-frequency branches attributed to O^{2-} (i.e., 8–23 THz) and O'^{2-} are shallower, than the ones for other $\text{Ln}_2\text{Zr}_2\text{O}_7$ pyrochlores. On the other hand, the branches corresponding to Zr^{4+} and low-frequency branches attributed to O^{2-} (i.e., 0–6 THz) are statistically invariant. Given that stronger interatomic bonding results in higher frequencies (for atoms of similar masses) [37], the above observation suggests that the interatomic bonds around La^{3+} be stronger than those around Nd^{3+} , Sm^{3+} , and Gd^{3+} cations while the bonding environment around Zr^{4+} basically remain the same for all $\text{Ln}_2\text{Zr}_2\text{O}_7$ pyrochlores.

For the phonon dispersion curves and PDOS shown in Fig. 3 for the $\text{Gd}_2\text{T}_2\text{O}_7$ pyrochlores, based on the features of the plots we can divide them into two pairs, i.e., ($\text{Gd}_2\text{Pb}_2\text{O}_7$, $\text{Gd}_2\text{Sn}_2\text{O}_7$) and ($\text{Gd}_2\text{Zr}_2\text{O}_7$, $\text{Gd}_2\text{Hf}_2\text{O}_7$). We can note that the phonon dispersions curves and PDOS show similar features for pyrochlores in the same pair, but are noticeably different for pyrochlores in different pairs. The above observation is understandable as Pb and Sn, and Zr and Hf, respectively are in the same element group possessing similar outermost valence configurations,

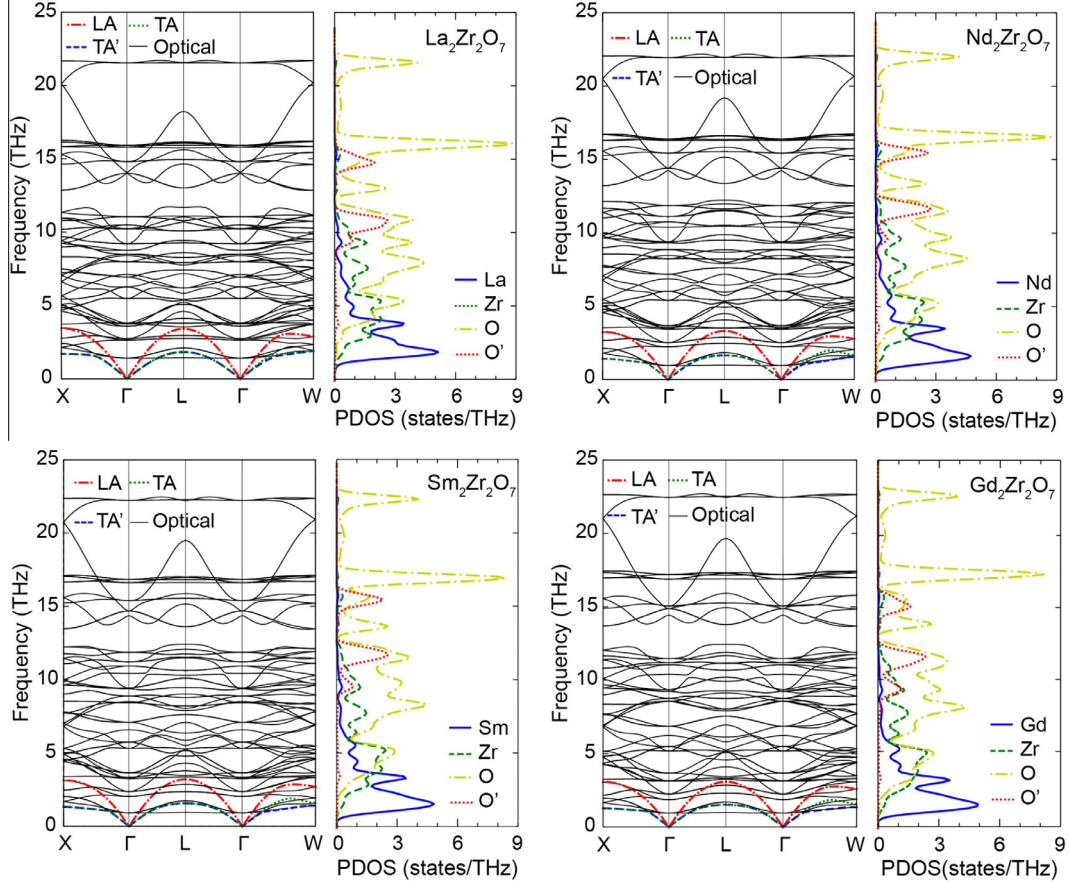


Fig. 2. Phonon dispersions and partial density of states (PDOS) for $\text{Ln}_2\text{Zr}_2\text{O}_7$ ($\text{Ln} = \text{La}, \text{Nd}, \text{Sm}, \text{Gd}$) pyrochlores. The two transverse (denoted as TA and TA') and one longitudinal (denoted as LA) acoustic phonon branches are indicated by green dotted, blue dashed and red dashed-dotted lines, respectively, while the optical branches are indicated by solid black lines. For the PDOS, the blue solid, green dashed, yellow dashed-dotted and red dotted curves denote those corresponding to Ln ($\text{Ln} = \text{Ln}, \text{Nd}, \text{Sm}, \text{Gd}$), Zr, O and O' atoms, respectively. (For interpretation of the references to colour in this figure legend, the reader is referred to the web version of this article.)

and thereby have similar bonding environments. The radii of T-type cations are as followed, 77.5 pm for Pb^{4+} , 72 pm for Zr^{4+} , 71 pm for Hf^{4+} and 69 pm for Sn^{4+} [61]. There is no apparent variation in the frequencies with respect to T-type cation radius. A possible reason for this difference is that most T-type cations exhibit nonmetal features, i.e., there is small electronegativity difference between T and O. Thus some of the T–O bonds show complex covalent characteristics rather than simple ionic features, and consequently the bond strength of T–O bonds cannot be simply determined by the cation radius.

Within the $(\text{Gd}_2\text{Pb}_2\text{O}_7, \text{Gd}_2\text{Sn}_2\text{O}_7)$ pair, $\text{Gd}_2\text{Sn}_2\text{O}_7$ has a much larger modulus than $\text{Gd}_2\text{Pb}_2\text{O}_7$ (Table 2) despite the radius of Sn^{4+} being smaller than that of Pb^{4+} . This implies that the $\text{Gd}_2\text{Sn}_2\text{O}_7$ has higher average interatomic bond strength than $\text{Gd}_2\text{Pb}_2\text{O}_7$. Consequently, compared to the branches of $\text{Gd}_2\text{Pb}_2\text{O}_7$, all the branches of $\text{Gd}_2\text{Sn}_2\text{O}_7$ show a shift toward higher frequencies, except for those attributed to Gd^{3+} , which stay essentially unchanged. On the other hand within the $(\text{Gd}_2\text{Zr}_2\text{O}_7, \text{Gd}_2\text{Hf}_2\text{O}_7)$ pair, the modulus of $\text{Gd}_2\text{Hf}_2\text{O}_7$ is slightly larger than that of $\text{Gd}_2\text{Zr}_2\text{O}_7$. A close examination of the plots in Figs. 3a and b reveals that $\text{Gd}_2\text{Hf}_2\text{O}_7$ exhibits higher-frequency O-branches, slightly lower-frequency T-branches, in comparison to $\text{Gd}_2\text{Zr}_2\text{O}_7$.

3.2.2. Grüneisen parameters

Using Eq. (8), we computed the dispersion of the Grüneisen parameters (γ) for all acoustic modes. The phonon dispersions, zoomed in for acoustic branches, and corresponding acoustic Grüneisen dispersion curves are shown in Figs. 4 and 5 $\text{Ln}_2\text{Zr}_2\text{O}_7$ and $\text{Gd}_2\text{T}_2\text{O}_7$ pyrochlores respectively. There are some general features we can note for both figures. We see the acoustic branches overlap with low-lying optical branches (also previously noted in Section 3.2.1). This results in mixing branches and nonlinear acoustic dispersion curves away from Γ point (the center of the Brillouin zone) [66], and leads to abrupt changes in γ due to avoided crossings between optical and acoustic branches (mostly TA branches). Besides the abrupt changes, there are also some small bumps along the Grüneisen dispersion curves (mostly for the LA branches), attributing to cases where acoustic branches cross the optical branches without losing linear features.

Examining the plots for $\text{Ln}_2\text{Zr}_2\text{O}_7$ pyrochlores shown in Fig. 4, we see that the acoustic phonon and Grüneisen dispersion curves are overall similar for different pyrochlores, except for that the TA and TA' branches of $\text{La}_2\text{Zr}_2\text{O}_7$ essentially overlap with each other whereas those of other zirconates diverse at one third of path from Γ to W point. In addition, we can see that the acoustic cut-off frequencies

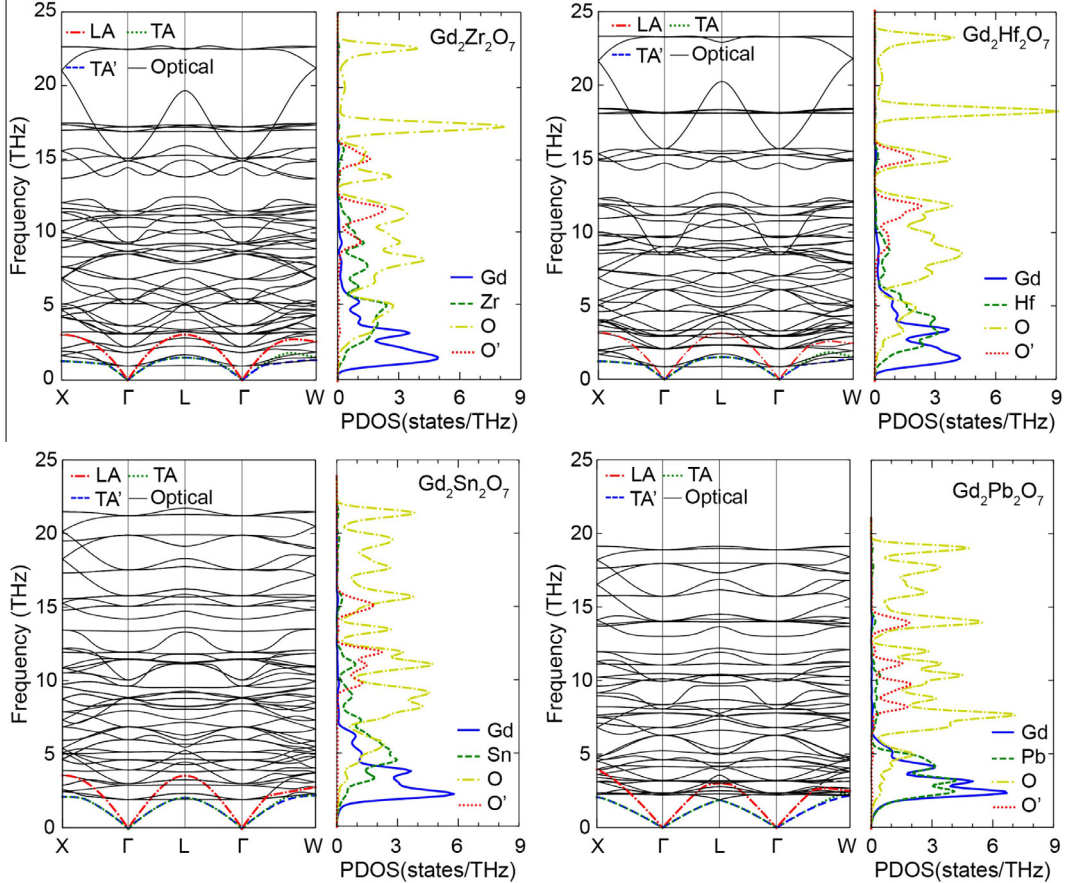


Fig. 3. Phonon dispersions and partial density of states (PDOS) for $\text{Gd}_2\text{T}_2\text{O}_7$ ($\text{T} = \text{Zr}, \text{Hf}, \text{Sn}, \text{Pb}$) pyrochlores. The two transverse (denoted as TA and TA') and one longitudinal (denoted as LA) acoustic phonon branches are indicated by green dotted, blue dashed and red dashed-dotted lines, respectively, while the optical branches are indicated by full black lines. For the PDOS, the blue solid, green dashed, yellow dashed-dotted and red dotted curves denote those corresponding to Gd, T ($\text{T} = \text{Zr}, \text{Hf}, \text{Sn}, \text{Pb}$), O and O' atoms, respectively. (For interpretation of the references to colour in this figure legend, the reader is referred to the web version of this article.)

at the zone boundaries decrease as the size of the Ln^{3+} cation decreases. Extremely high γ values (above ~ 10) appear at the TA/TA' branches in $\text{Ln}_2\text{Zr}_2\text{O}_7$ pyrochlores, indicating that TA/TA' branches are strongly scattered by low-lying optical branches and thereby do not contribute much to thermal conduction.

For the set of $\text{Gd}_2\text{T}_2\text{O}_7$ pyrochlores (cf. Fig. 5), we see that $\text{Gd}_2\text{Hf}_2\text{O}_7$ and $\text{Gd}_2\text{Zr}_2\text{O}_7$ exhibit similar dispersion curves. Like $\text{Ln}_2\text{Zr}_2\text{O}_7$ pyrochlores, the Grüneisen dispersion curves of $\text{Gd}_2\text{Hf}_2\text{O}_7$ and $\text{Gd}_2\text{Zr}_2\text{O}_7$ show abrupt changes in γ and extremely high values of γ at the TA/TA' branches where avoided crossings occur. In comparison, $\text{Gd}_2\text{Zr}_2\text{O}_7$ and $\text{Gd}_2\text{Hf}_2\text{O}_7$ exhibit much less variation in γ for the TA/TA' branches. This is because that the lowest optical branches of $\text{Gd}_2\text{Pb}_2\text{O}_7$ and $\text{Gd}_2\text{Sn}_2\text{O}_7$ are located at ~ 2 THz, higher than those of $\text{Gd}_2\text{Zr}_2\text{O}_7$ and $\text{Gd}_2\text{Hf}_2\text{O}_7$ (located at ~ 1 THz), so that their TA/TA' branches are able to better retain acoustic feature even near the boundary of Brillouin zone, showing smaller γ values. Fundamentally the difference between the ($\text{Gd}_2\text{Zr}_2\text{O}_7$, $\text{Gd}_2\text{Hf}_2\text{O}_7$) and ($\text{Gd}_2\text{Pb}_2\text{O}_7$, $\text{Gd}_2\text{Sn}_2\text{O}_7$) pairs can be attributed to the fact that $\text{Gd}_2\text{Zr}_2\text{O}_7$ and $\text{Gd}_2\text{Hf}_2\text{O}_7$ exhibit strong ionic characters while $\text{Gd}_2\text{Pb}_2\text{O}_7$ and $\text{Gd}_2\text{Sn}_2\text{O}_7$ are of more covalent bonding features. On the other hand, the elevation of the low-lying optical branches in the cases of $\text{Gd}_2\text{Pb}_2\text{O}_7$ and $\text{Gd}_2\text{Sn}_2\text{O}_7$ seemingly leads to more

interference between those optical branches with the LA branch. This is particularly noticeable in the case of $\text{Gd}_2\text{Sn}_2\text{O}_7$ where we can note a clear deflection in the LA branch between Γ and W that causes an abrupt change in γ_{LA} (cf. Fig. 5).

From the phonon and Grüneisen dispersion curves, the average Grüneisen parameters $\bar{\gamma}_i$ ($i = \text{TA}, \text{TA}'$ or LA) (using Eq. (9)), along with the phonon velocities and reduced Debye temperatures, are then calculated for each acoustic branch, shown in Table 3. We can see that for the $\text{Ln}_2\text{Zr}_2\text{O}_7$ group and $\text{Gd}_2\text{Hf}_2\text{O}_7$, the TA and TA' branches exhibit much larger values of the average Grüneisen parameter than the LA branch, while for $\text{Gd}_2\text{Pb}_2\text{O}_7$ and $\text{Gd}_2\text{Sn}_2\text{O}_7$ the three acoustic phonon branches show comparable values of the average Grüneisen parameter. Another observation from Table 3 is that $\text{La}_2\text{Zr}_2\text{O}_7$ exhibits significantly lower $\bar{\gamma}_{\text{TA}}/\bar{\gamma}_{\text{TA}'}$ than other $\text{Ln}_2\text{Zr}_2\text{O}_7$ pyrochlores.

3.3. Prediction of thermal conductivities

Table 4 shows the thermal conductivities predicted by the RTA model (cf. Eq. (3)), the minimum thermal conductivities (κ_{\min}) estimated from Clarke's and Cahill's models, and the experimental data. For the $\text{Ln}_2\text{Zr}_2\text{O}_7$ pyrochlores, we see that the predicted values of κ_{\min} from Clarke's and

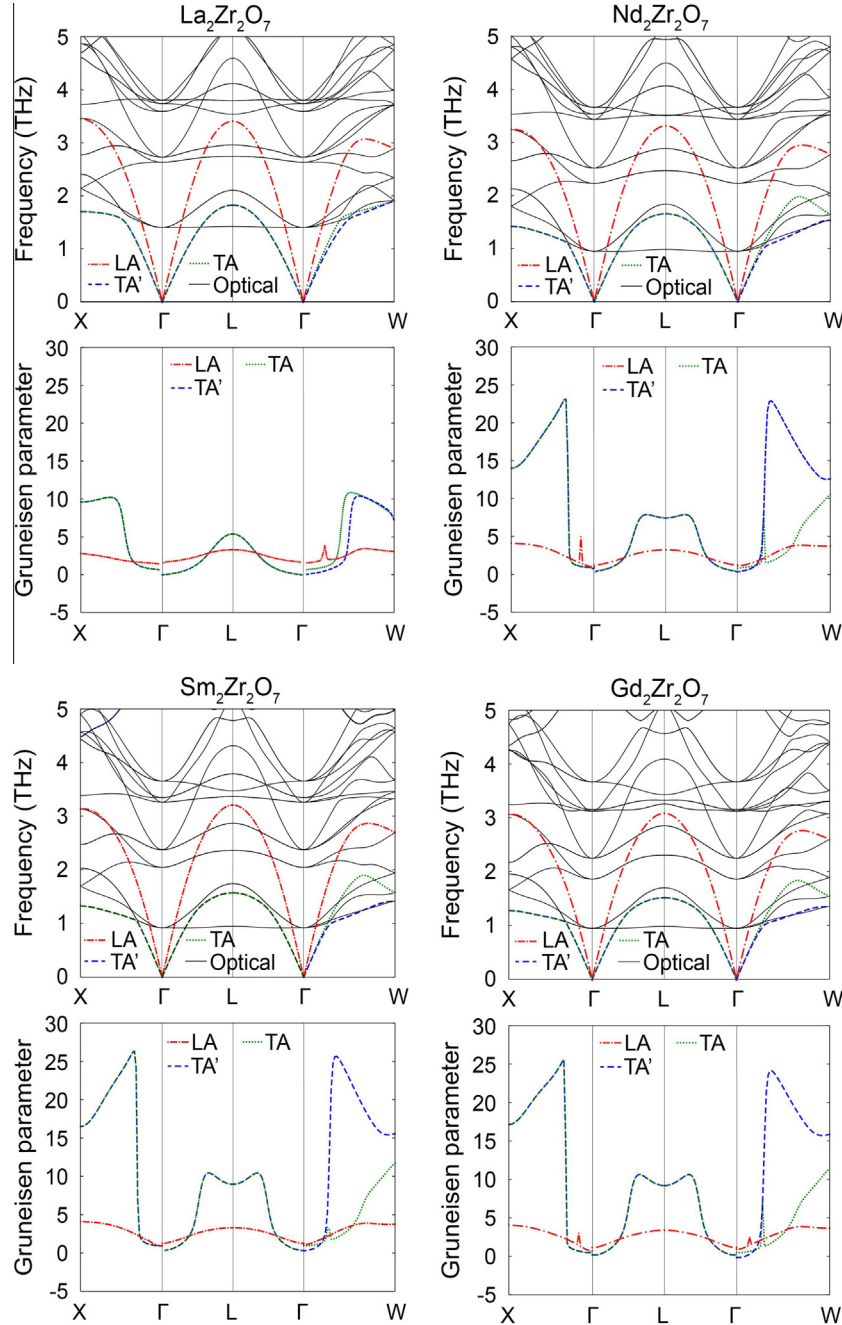


Fig. 4. Calculated phonon dispersions (zoom in for the acoustic branches, i.e., TA, TA', LA and optical branches indicated by green dotted, blue dashed, red dashed-dotted and solid black lines, respectively) and corresponding acoustic Grüneisen parameters for $\text{Ln}_2\text{Zr}_2\text{O}_7$ ($\text{Ln} = \text{La}, \text{Nd}, \text{Sm}, \text{Gd}$) pyrochlores. (For interpretation of the references to colour in this figure legend, the reader is referred to the web version of this article.)

Cahill's models are almost the same, which is expected given similar lattice constants, moduli (and thus sound velocities) and densities across the pyrochlores. This is apparently inconsistent with the trend revealed in the experimental data [15,17,19,67], mostly showing an order of $\kappa_{\text{La}_2\text{Zr}_2\text{O}_7} > \kappa_{\text{Nd}_2\text{Zr}_2\text{O}_7} > \kappa_{\text{Sm}_2\text{Zr}_2\text{O}_7} > \kappa_{\text{Gd}_2\text{Zr}_2\text{O}_7}$ [68]. On the other hand, our predictions using the RTA model shows good agreement in both the values of κ and trend with the experimental data for the $\text{Ln}_2\text{Zr}_2\text{O}_7$ pyrochlores. Additionally we can see from the data shown in Table 4 that only LA branches in $\text{Ln}_2\text{Zr}_2\text{O}_7$ pyrochlores are effective to carry heat while the two transverse branches yield negligible contributions ($<0.1 \text{ W m}^{-1} \text{ K}^{-1}$) to the thermal

conductivity. The trivial contribution to κ from the transverse branches directly derives from the large values of $\bar{\gamma}_{\text{TA}}$ and $\bar{\gamma}_{\text{TA}'}$ (cf. Table 3). Meanwhile it is worth noting that, though much smaller than $\bar{\gamma}_{\text{TA}}$ and $\bar{\gamma}_{\text{TA}'}$, $\bar{\gamma}_{\text{LA}}$ exhibits a sizable magnitude (2–3), higher than the usual average Grüneisen parameters (often being 1–2) of most other systems [69].

Within the $\text{Gd}_2\text{T}_2\text{O}_7$ pyrochlore group, the LA branches also dominate the thermal conductivity for $\text{Gd}_2\text{Zr}_2\text{O}_7$ and $\text{Gd}_2\text{Hf}_2\text{O}_7$. Particularly for $\text{Gd}_2\text{Hf}_2\text{O}_7$, it has a low value of $\bar{\gamma}_{\text{LA}}$ (i.e., 1.99) despite very large values of $\bar{\gamma}_{\text{TA}}$ and $\bar{\gamma}_{\text{TA}'}$ (both beyond 8), and thus yield a relatively high κ value. Unlike $\text{Gd}_2\text{Zr}_2\text{O}_7$ and $\text{Gd}_2\text{Hf}_2\text{O}_7$, $\text{Gd}_2\text{Pb}_2\text{O}_7$ and $\text{Gd}_2\text{Sn}_2\text{O}_7$ exhibit much lower $\bar{\gamma}_{\text{TA}}$ and $\bar{\gamma}_{\text{TA}'}$ values, even

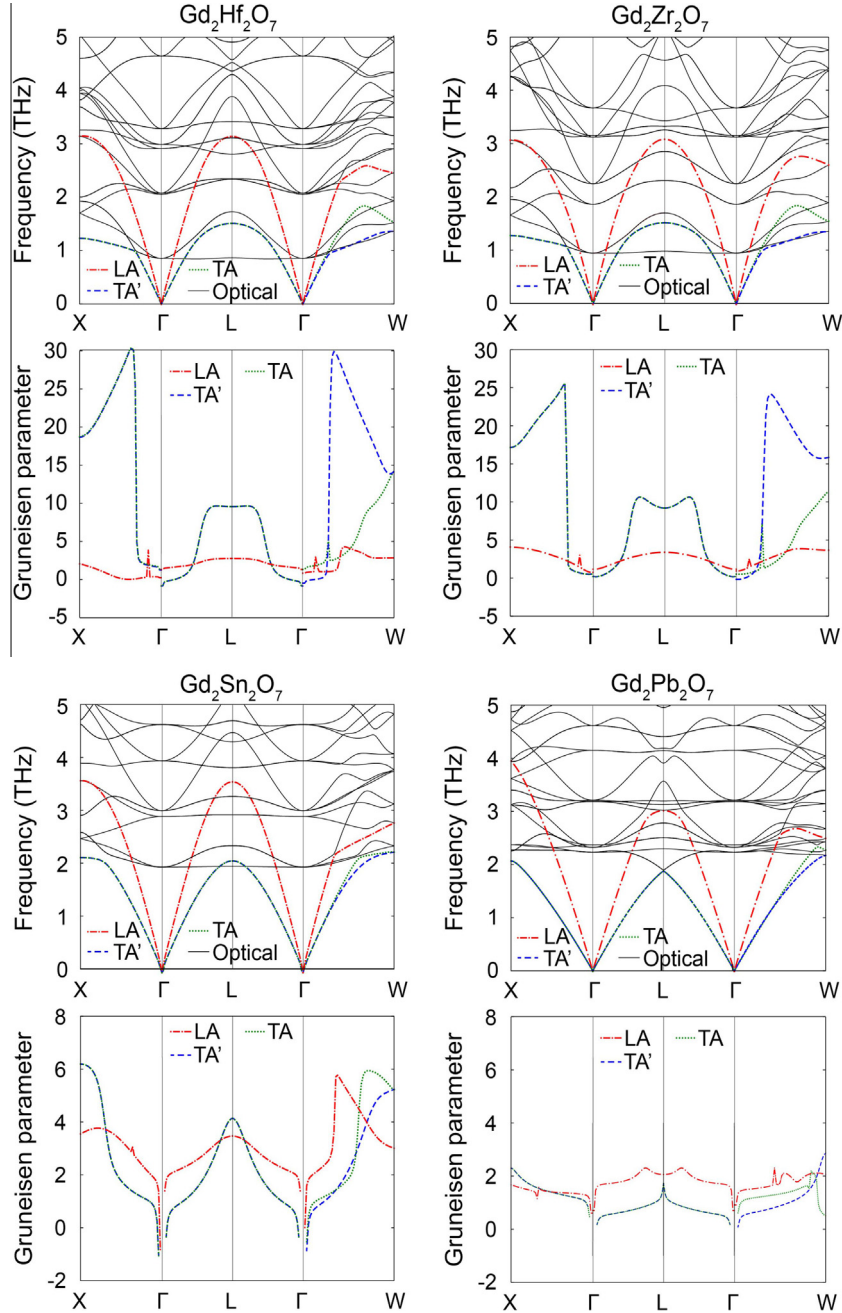


Fig. 5. Calculated phonon dispersions (zoom in for the acoustic branches, i.e., TA, TA', LA and optical branches, indicated by green dotted, blue dashed, red dashed-dotted and solid black lines, respectively) and corresponding acoustic Grüneisen parameters for $\text{Gd}_2\text{T}_2\text{O}_7$ ($\text{T} = \text{Zr}, \text{Hf}, \text{Sn}, \text{Pb}$) pyrochlores. (For interpretation of the references to colour in this figure legend, the reader is referred to the web version of this article.)

lower than $\bar{\gamma}_{LA}$. As a consequence, the TA/TA' branches of $\text{Gd}_2\text{Pb}_2\text{O}_7$ and $\text{Gd}_2\text{Sn}_2\text{O}_7$ become important in heat conduction though their contributions, i.e., κ_{TA} and $\kappa_{TA'}$, remain smaller than the one by the LA branch, κ_{LA} because of their smaller sound velocity and reduced Debye temperature. One thing to note is that $\text{Gd}_2\text{Pb}_2\text{O}_7$, with overall low average Grüneisen parameters, is predicted to yield the highest κ (i.e., $3.65 \text{ W m}^{-1} \text{ K}^{-1}$) among all these pyrochlores considered according to the RTA model. This is in sharp contrast with the predictions from Clarke's and Cahill's model, both suggesting that $\text{Gd}_2\text{Pb}_2\text{O}_7$ have the lowest κ because of its small phonon velocities and moduli. Another thing to note is that the $\text{Gd}_2\text{Sn}_2\text{O}_7$ exhibit largest

$\bar{\gamma}_{LA}$ and thus yield a rather small κ albeit somewhat small $\bar{\gamma}_{TA}$ and $\bar{\gamma}_{TA'}$.

In Fig. 6, we compare the predictions of κ from the RTA model with the available experimental data over the temperature range of 600 K–1600 K for the RE pyrochlores (abate $\text{Gd}_2\text{Hf}_2\text{O}_7$ and $\text{Gd}_2\text{Pb}_2\text{O}_7$ due to absence of experimental data). All experimental data presented are effective thermal conductivities of fully dense materials [67,70]. In general we can see that our predictions agree well with the experimental data. However there are some discrepancies between the predicted and experimentally measured κ values at low (i.e., $600 \text{ K} < T < 800 \text{ K}$) and high (i.e., $T > 1400 \text{ K}$) temperatures for the $\text{Ln}_2\text{Zr}_2\text{O}_7$

Table 3. Average longitudinal (v_{LA}) and transverse ($v_{TA/TA'}$) phonon velocities, average Grüneisen parameters $\bar{\gamma}_i$ ($i = TA$, TA' or LA), reduced Debye temperatures ($\tilde{\Theta}_{LA}$ and $\tilde{\Theta}_{TA/TA'}$) calculated from phonon dispersions (cf. Figs. 4 and 5). The phonon velocity is taken as the slope of each acoustic branch close to the Γ point while the reduced Debye temperature is computed using Eqs. (5), (6).

	$\bar{\gamma}_{LA}$	$\bar{\gamma}_{TA}$	$\bar{\gamma}'_{TA}$	v_{LA}	$v'_{TA/TA'}$	$\tilde{\Theta}_{LA}$	$\tilde{\Theta}_{TA/TA'}$
La ₂ Zr ₂ O ₇	2.48	4.87	4.35	5878	3125	256	136
Nd ₂ Zr ₂ O ₇	2.75	6.23	10.10	5906	3126	260	138
Sm ₂ Zr ₂ O ₇	2.81	7.40	11.98	5783	3086	256	137
Gd ₂ Zr ₂ O ₇	2.75	7.19	11.57	5634	3059	252	137
Gd ₂ Hf ₂ O ₇	1.99	8.07	12.53	5105	2787	229	125
Gd ₂ Pb ₂ O ₇	1.73	1.18	1.06	4463	2450	195	107
Gd ₂ Sn ₂ O ₇	3.19	2.68	2.46	5388	3178	242	142

pyrochlore group. These discrepancies are because the Umklapp scattering is assumed to dominate the thermal resistance. Particularly in the low temperature regime, the predicted κ values are generally higher than the experimental measurements, i.e., the RTA model overestimates the thermal conductivity. This overestimation may come from the fact that the samples in experiments are polycrystalline with considerable amount of lattice defects that induce extra phonon scattering [32] to lower the thermal conductivity. In the high temperature regime, the experimental κ values exhibit slower downward trend or even slightly increase, which can be due to high-temperature radiation that provides positive contribution to thermal conductivity [32] and thereby offsets the downward trend attributed to Umklapp scattering processes. One exception in Fig. 6 is the case of Gd₂Sn₂O₇ where the RTA model prediction is shown to capture the correct temperature dependence of κ but somewhat underestimate the magnitude. However the statistical significance of the above comparison for Gd₂Sn₂O₇ is questionable given the insufficient experimental data (cf. Fig. 6f). The contributions of defects at low temperatures and radiation at high temperatures moderate the temperature dependence of the intrinsic thermal conductivity, leading to the flatness in experimental κ vs. T curves.

To compare the thermal conductivities between different RE pyrochlores, the predicted κ versus temperature curves (from the RTA model) are plotted together for the Ln₂Zr₂O₇ and Gd₂T₂O₇ pyrochlore groups in Fig. 7a and b respectively. Furthermore, we define a relative ratio ρ_κ of thermal conductivity, taking Gd₂Zr₂O₇ as the reference:

$$\rho_\kappa = \frac{\kappa_{Ln_2T_2O_7} - \kappa_{Gd_2Zr_2O_7}}{\kappa_{Gd_2Zr_2O_7}} \quad (10)$$

Table 4. Calculated minimum thermal conductivity (κ_{min} , $\text{W m}^{-1} \text{K}^{-1}$) from Clarke's and Cahill's model; Calculated thermal conductivity (κ , $\text{W m}^{-1} \text{K}^{-1}$) from the RTA model (cf. Eqs. (3), (4)) at 1073 K; Experimental thermal conductivity at 1073 K ($\kappa_{Exp.}$, $\text{W m}^{-1} \text{K}^{-1}$).

	κ from the RTA model at 1073 K					$\kappa_{Exp.}$ at 1073 K				
	Clarke's	Cahill's	LA	TA	TA'	Total	Liu [17]	Lehmann [19]	Suresh [15]	Pan [67]
La ₂ Zr ₂ O ₇	1.21	1.14	1.58	0.06	0.07	1.72		1.55	1.43	
Nd ₂ Zr ₂ O ₇	1.23	1.16	1.36	0.04	0.01	1.41	1.48	1.24		
Sm ₂ Zr ₂ O ₇	1.23	1.16	1.26	0.03	0.01	1.30	1.44			1.20
Gd ₂ Zr ₂ O ₇	1.22	1.15	1.26	0.03	0.01	1.30	1.33		1.03	1.18
Gd ₂ Hf ₂ O ₇	1.07	1.06	2.31	0.02	0.01	2.34				
Gd ₂ Pb ₂ O ₇	0.92	0.88	2.06	0.71	0.88	3.65				
Gd ₂ Sn ₂ O ₇	1.17	1.16	0.90	0.25	0.30	1.45				

where $\kappa_{Ln_2T_2O_7}$ and $\kappa_{Gd_2Zr_2O_7}$ are the RTA model predicted thermal conductivities for Ln₂T₂O₇ (Ln = La, Nd, Sm, Gd and T = Zr, Hf, Sn, Pb) and Gd₂Zr₂O₇ respectively. Fig. 7c and d shows the plots of ρ_κ versus the Ln³⁺ and T⁴⁺ cation radius respectively with the error bar indicating the standard deviation of ρ_κ with respect to the temperature. The values of ρ_κ for experimental data were also calculated, in the same way as Eq. (10) but with the predicted values replaced by experimental values. Here only those experimental studies that contain measurements of Gd₂Zr₂O₇ and other pyrochlores simultaneously were considered, to avoid errors due to experimental methods and samples. The usage of the relative ratio ρ_κ helps moderate the radiated and spurious effects during to scattered data in experiments to enable a more accurate and quantitative comparison between the experimental measurements with our predictions. For the Ln₂Zr₂O₇ pyrochlore group where experimental data are available, the predicted and experimental ρ_κ values show a close match (cf. Fig. 7c). This good agreement further evidences that the RTA model captures the essential physics underlying thermal transport in RE pyrochlores. In addition, there is an apparent increasing trend in ρ_κ as the Ln³⁺ cation radius increases. For the Gd₂T₂O₇ pyrochlore group, the experimental ρ_κ values are not available. Our predictions suggest that, when measured under same experimental conditions, Gd₂Sn₂O₇ would yield a similar κ value as Gd₂Zr₂O₇, but much smaller than the ones of Gd₂Hf₂O₇ and Gd₂Pb₂O₇, thus being a potential TBC material like Gd₂Zr₂O₇.

The above predicted effects of Ln³⁺ and T⁴⁺ cations on the thermal conductivity show certain qualitative similarity with the molecular dynamic (MD) study by Schelling *et al.* [71] which also reveals that the T⁴⁺ cation plays a more important role than the Ln³⁺ cation. However, in the study by Schelling *et al.*, simple parameterized ionic potentials were used to describe the interatomic bonding and the T-O bond strength was directly correlated with the size of the T⁴⁺ cation, not accounting for the actual bonding characteristics (i.e., ionic or covalent). This rough simplification is questionable as the covalent characteristics may play a critical role in determining the bond strength of the T-O bond (see Section 3.2.1).

3.4. Structural origin of low-lying optical branches

Clearly evidenced from our results above, the low-lying optical phonon branches play a critical role in determining the thermal conductivities of RE pyrochlores. They strongly scatter the acoustic branches, leading to extremely large Grüneisen parameters (cf. Figs. 4 and 5 and Table 3)

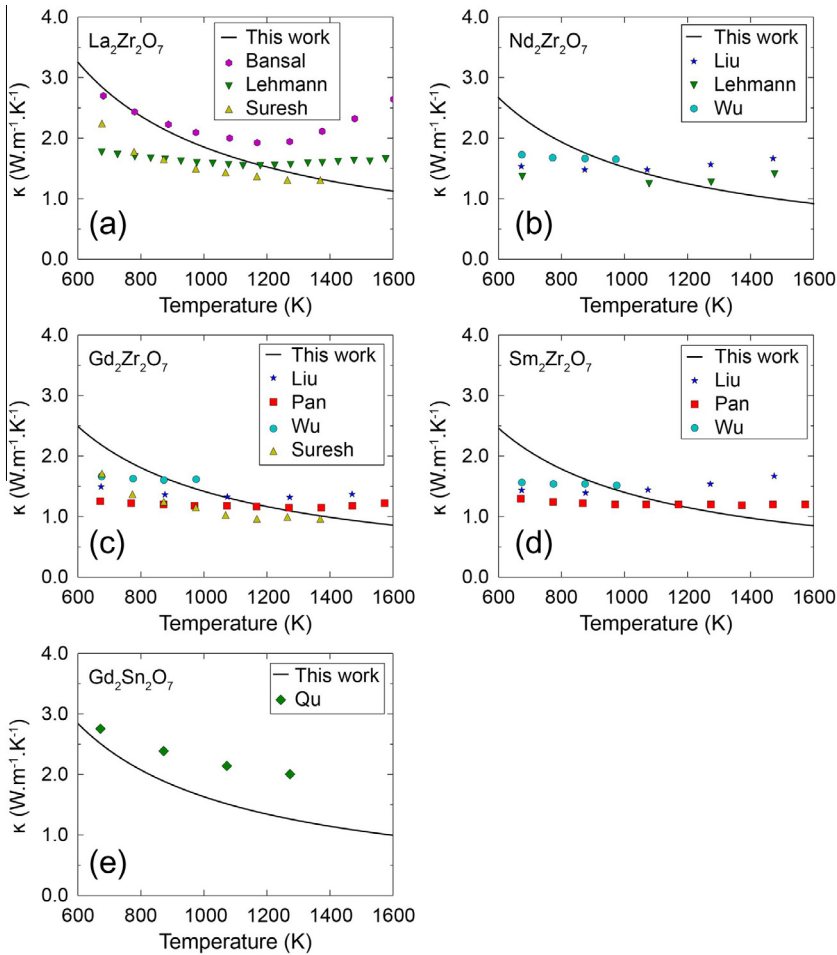


Fig. 6. Lattice thermal conductivities (κ) of $\text{Ln}_2\text{Zr}_2\text{O}_7$ ($\text{Ln} = \text{La}, \text{Nd}, \text{Sm}, \text{Gd}$) and $\text{Gd}_2\text{Sn}_2\text{O}_7$. The solid red lines represent the predicted values of κ using the RTA model. The various filled symbols represent the experimental measurements from Bansal et al. [14] (hexagon), Lehmann et al. [19] (down triangle), Suresh et al. [15] (up triangle), Liu et al. [17] (star), Pan et al. [67] (square), Wu et al. [16] (circle) and Qu et al. [72] (diamond), respectively. The experimental data for $\text{Gd}_2\text{Hf}_2\text{O}_7$ and $\text{Gd}_2\text{Pb}_2\text{O}_7$ are missing. (For interpretation of the references to colour in this figure legend, the reader is referred to the web version of this article.)

and subsequently low κ values. As we already know from Section 3.2.1, the low-lying optical branches are attributed to the vibrations of the Ln atom. A close examination of the vibrational patterns responsible for the low-lying optical branches reveals that Ln exhibits sizable vibrational magnitude while the O' (8b) atom shows near zero vibration, and T and O (48f) atoms show very small amplitude of vibration, mostly lesser than 15% of that of the Ln atom. Particularly for the Ln atom, there exist two possible modes of vibration associated with the low-lying optical branches at X , Γ and L points, one being that Ln moves in-plane (i.e., on the perpendicular to the O'-Ln bond, cf. Fig. 8) toward the adjacent O (48f) atom while the other being that Ln is displaced toward one of the nearest T atoms, as illustrated in Fig. 8.

The large vibrational magnitude of Ln is a direct consequence of loose bonds between Ln and its adjacent atoms. In this regard, we examined the charge distribution around the Ln atom to further elucidate its bonding environment. Since the bonds within the RE pyrochlores mostly exhibit ionic features, the Voronoi deformation density (VDD) method [73] was employed to analyze atomic static charges. Compared to other charge-analyzing methods, the VDD method has the advantage of giving chemically meaningful

charges with basis-set independency [73]. The calculated static charges using VDD for Ln, T, O (48f) and O' (8b) atoms are presented in Fig. 9a and b for $\text{Ln}_2\text{Zr}_2\text{O}_7$ ($\text{Ln} = \text{La}, \text{Nd}, \text{Sm}, \text{Gd}$) and $\text{Gd}_2\text{T}_2\text{O}_7$ ($T = \text{Zr}, \text{Hf}, \text{Sn}, \text{Pb}$) pyrochlores respectively.

For the $\text{Ln}_2\text{Zr}_2\text{O}_7$ pyrochlore group, the charge at the Ln site increases as the cation radius increases while in accordance the charges at O (48f) and O' (8b) become more negative. This indicates that Ln loses electrons more easily (to its neighboring O (48f) and O' (8b) atoms) as the cation radius increases. However we can see from Fig. 9a that the charge change at O (48f) is rather negligible, suggesting that the charge transfer mainly occurs between Ln and O' (8b), which is not surprising with O' (8b) sites being the nearest neighbors to Ln. Apparently the net increase in charge transfer from Ln to surrounding atoms may contribute to enhancing the local ionic interactions. This provides a possible explanation for the elevation of optical branches and lower $\bar{\gamma}_{TA}/\bar{\gamma}_{TA'}$ of $\text{La}_2\text{Zr}_2\text{O}_7$ in comparison to other $\text{Ln}_2\text{Zr}_2\text{O}_7$ pyrochlores. Meanwhile the charge at Zr remains largely invariant irrespective of the species of Ln. This together with the minimal change in the charges of O (48f) sites indicates that the bonding environment around Zr remains mostly unchanged, and thus explains the

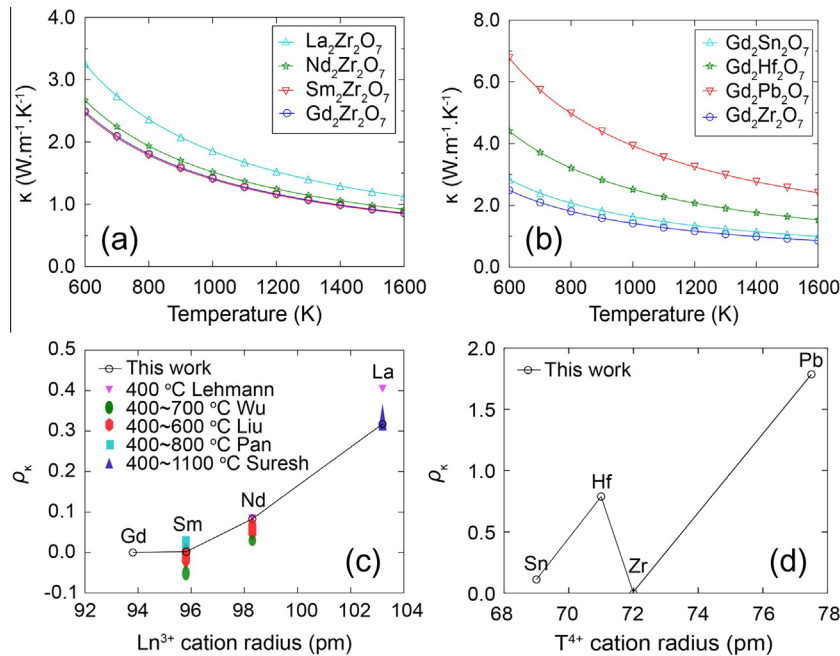


Fig. 7. Predicted thermal conductivities (κ) for (a) $\text{Ln}_2\text{Zr}_2\text{O}_7$ and (b) $\text{Gd}_2\text{T}_2\text{O}_7$ pyrochlore groups respectively. The relative ratio of thermal conductivity (ρ_κ) taking $\text{Gd}_2\text{Zr}_2\text{O}_7$ as the reference (cf. Eq. (10)), are plotted versus the (c) Ln^{3+} and (d) T^{4+} cation radius respectively.

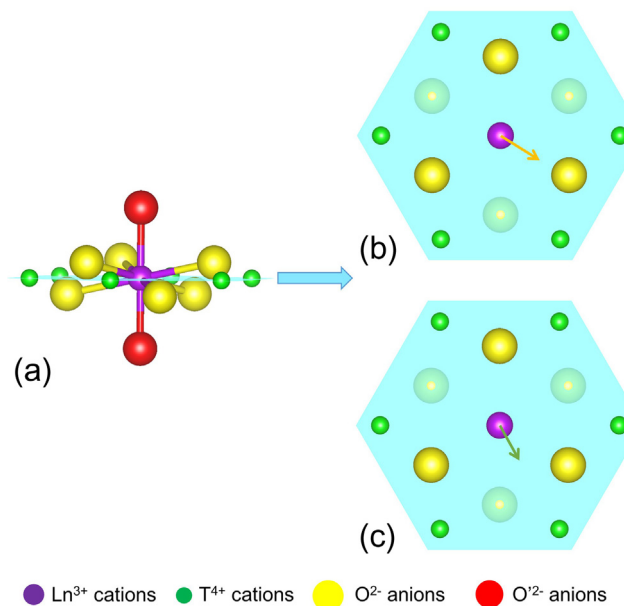


Fig. 8. (a) Schematic showing the bonding environment around the Ln ($16d$) atom, showing nearest six O ($48f$), two O' ($8b$) and six Zr ($16c$). The cyan plane indicates the plane that cuts through Ln and is perpendicular to the $\text{O}'-\text{Ln}$ bond. The projection views of the two possible vibrational motions (associated with low-lying frequencies) of the Ln atom, i.e., (b) Ln moving in-plane toward the adjacent O ($48f$) atom, and (c) Ln moving toward to one of the nearest T atoms, are illustrated with vibrational directions indicated by the yellow and green arrows respectively. (For interpretation of the references to colour in this figure legend, the reader is referred to the web version of this article.)

invariance of the branches corresponding to Zr^{4+} shown in Fig. 2.

Meanwhile for the $\text{Gd}_2\text{T}_2\text{O}_7$ pyrochlore group (Fig. 9b), the Zr and Hf sites exhibit charge values ~ 3 while the Sn

and Pb sites exhibit charge values close to 2, and accordingly the O ($48f$) sites neighboring $\text{Gd}_2\text{Sn}_2\text{O}_7$ and $\text{Gd}_2\text{Pb}_2\text{O}_7$ show less negative charges compared to the ones in $\text{Gd}_2\text{Zr}_2\text{O}_7$ and $\text{Gd}_2\text{Hf}_2\text{O}_7$. These large discrepancies in charge values directly evidence the less ionicity but more covalency in the characteristics of $\text{T}-\text{O}$ bonds in $\text{Gd}_2\text{Sn}_2\text{O}_7$ and $\text{Gd}_2\text{Pb}_2\text{O}_7$ than $\text{Gd}_2\text{Zr}_2\text{O}_7$ and $\text{Gd}_2\text{Hf}_2\text{O}_7$, as previously mentioned in Section 3.2.1. The above difference is also well reflected in Fig. 10 where we see the charge center of O ($48f$) anion stay close to its neighboring T cations in the cases of $\text{T} = \text{Zr}$ and Hf while drift toward the Gd cation in the cases of $\text{T} = \text{Sn}$ and Pb . Although from the charges at Ln and O' ($8b$) are barely affected by the presence of different T atoms (cf. Fig. 9b), the proximity of O ($48f$) charge centers to Gd in $\text{Gd}_2\text{Sn}_2\text{O}_7$ and $\text{Gd}_2\text{Pb}_2\text{O}_7$ will strengthen the $\text{Gd}-\text{O}$ ($48f$) bonds. The stronger bonding explains the elevation of the low-lying optical branches (corresponding to Gd vibrations) and significantly smaller $\bar{\gamma}_{TA}/\bar{\gamma}_{TA'}$ for $\text{Gd}_2\text{Sn}_2\text{O}_7$ and $\text{Gd}_2\text{Pb}_2\text{O}_7$ (cf. Fig. 4).

The above structural origin underlying low-lying optical branches provides intuitive insights toward understanding lattice thermal conductance in RE pyrochlores. For instance, $\text{Gd}_2\text{Pb}_2\text{O}_7$ has the lowest overall bond strength (moduli) among those RE pyrochlore systems but meanwhile has strong $\text{Gd}-\text{O}$ ($48f$) bonds which induce elevated low-lying optical branches that have less interference with the transport of acoustic phonons. As such, $\text{Gd}_2\text{Pb}_2\text{O}_7$ exhibits a relatively high thermal conductivity. Nonetheless, it is worth pointing out that the elevation of low-lying optical branches does not always favor the transport of acoustic phonons. As seen in the case of $\text{Gd}_2\text{Sn}_2\text{O}_7$, though inducing less scattering in the TA/TA' branches, the elevated optical branches cause considerable scattering in the LA branch which is of higher frequency than TA branches, leading to a rather low thermal conductivity (cf. Fig. 5 and Table 4). Thus further studies are necessary to clarify the competition between TA/TA' scattering and

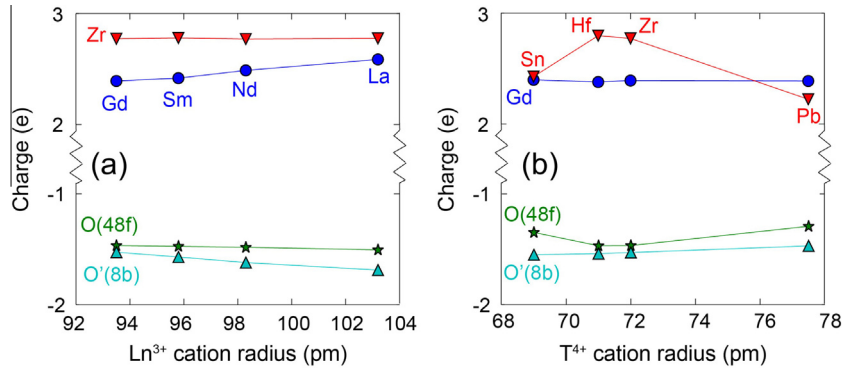


Fig. 9. Calculated static charges at different atom sites (with the VDD method) for (a) $\text{Ln}_2\text{Zr}_2\text{O}_7$ and (b) $\text{Gd}_2\text{T}_2\text{O}_7$ pyrochlores, respectively.

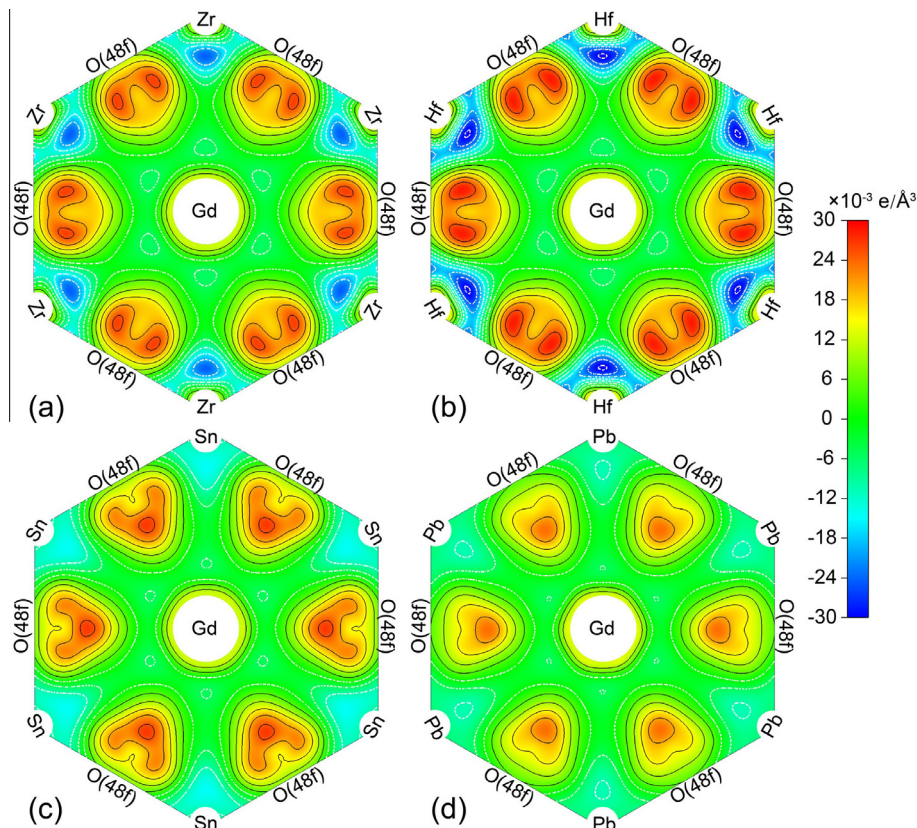


Fig. 10. Calculated deformation charge density contours on the planes cutting through Gd and perpendicular to the O'-Gd bond for (a) $\text{Gd}_2\text{Zr}_2\text{O}_7$, (b) $\text{Gd}_2\text{Hf}_2\text{O}_7$, (c) $\text{Gd}_2\text{Sn}_2\text{O}_7$ and (d) $\text{Gd}_2\text{Pb}_2\text{O}_7$ pyrochlores, respectively. The contours are taken at intervals of $0.005 \text{ e}/\text{\AA}^3$. The solid black contours and red color represent positive values (gaining electrons), while the white dash contours and blue color correspond to negative values (losing electrons). (For interpretation of the references to colour in this figure legend, the reader is referred to the web version of this article.)

LA scattering, to fully understand the role of low-lying optical branches in thermal conductance in RE pyrochlores.

4. Summary

In summary, the phonon properties and thermal conductivities of two sets of RE pyrochlores, $\text{Ln}_2\text{Zr}_2\text{O}_7$ ($\text{Ln} = \text{La}, \text{Nd}, \text{Sm}, \text{Gd}$) and $\text{Gd}_2\text{T}_2\text{O}_7$ ($\text{T} = \text{Zr}, \text{Hf}, \text{Sn}, \text{Pb}$) have been studied through density functional theory calculations and quasi harmonic approximation, combining the relaxation-time approximation (RTA) together with the Debye model. Compared to the often-used minimum

thermal conductivity approach using Clarke's and Cahill's models that hardly differential different RE pyrochlores, the RTA with the Debye model yields much more accurate predictions of thermal conductivities of RE pyrochlores, validated by available experimental measurements. In particular, for the $\text{Ln}_2\text{Zr}_2\text{O}_7$ pyrochlores, the thermal conductivity is predicted to increase as the Ln^{3+} cation radius increases, in close agreement with experiments.

Our results indicate that the low thermal conductivities of RE pyrochlores mainly derive from the interference between the low-lying optical branches and acoustic branches. For the $\text{Ln}_2\text{Zr}_2\text{O}_7$ pyrochlore group and $\text{Gd}_2\text{Hf}_2\text{O}_7$, the low-lying optical phonon branches cause

significant scattering of the transverse acoustic branches, leading to very large Grüneisen parameters and rendering the transverse branches largely irrelevant in lattice thermal conductance. In comparison, $\text{Gd}_2\text{Pb}_2\text{O}_7$ and $\text{Gd}_2\text{Sn}_2\text{O}_7$ exhibit much elevated low-lying optical phonon branches and therefore much less scattering in the transverse branches. Consequently the transverse branches produce decent contributions to the thermal conductivity. The above interplay between the low-lying optical branches and transverse branches in different RE pyrochlores, i.e., $\text{Ln}_2\text{T}_2\text{O}_7$ ($\text{Ln} = \text{La}, \text{Nd}, \text{Sm}, \text{Gd}$, $\text{T} = \text{Zr}, \text{Hf}, \text{Sn}, \text{Pb}$), is shown to originate from the bonding between the Ln and its adjacent O atoms where the bonding strength is affected by the charge transfer between Ln and O° (8b) atoms as well as the shifting of the O (48f) charge centers. Meanwhile, our study also indicated that the low-lying optical phonon branches, when elevated, may induce substantial scattering in the longitude acoustic branch of the RE pyrochlores, suggesting that further studies are necessary to clarify the playoff between scattering processes in transverse and longitude acoustic branches in order to fully elucidate the role of low-lying optical branches in determining the thermal conductivity in RE pyrochlores.

Acknowledgement

We greatly thank the financial support from McGill Engineering Doctoral Award and National Sciences and Engineering Research Council (NSERC) Engage grant (Grant # EGP 452480-13) and Discovery grant (Grant # RGPIN 418469-2012). We also acknowledge Supercomputer Consortium Laval UQAM McGill and Eastern Quebec for providing computing power.

References

- [1] B. Gleeson, J. Propul. Power 22 (2006) 375.
- [2] D.R. Clarke, C.G. Levi, Ann. Rev. Mater. Res. 33 (2003) 383.
- [3] A.G. Evans, D.R. Clarke, C.G. Levi, J. Eur. Ceram. Soc. 28 (2008) 1405.
- [4] C.G. Levi, Curr. Opin. Solid State Mater. Sci. 8 (2004) 77.
- [5] M.R. Winter, D.R. Clarke, J. Am. Ceram. Soc. 90 (2007) 533.
- [6] C. Mercer, J.R. Williams, D.R. Clarke, A.G. Evans, Proc. Royal Soc. A Math. Phys. Eng. Sci. 463 (2007) 1393.
- [7] M. Watanabe, C. Mercer, C.G. Levi, A.G. Evans, Acta Mater. 52 (2004) 1479.
- [8] O. Fabrichnaya, F. Aldinger, Z. Metallk. 95 (2004) 27.
- [9] U. Schulz, J. Am. Ceram. Soc. 83 (2000) 904.
- [10] R.G. Hutchinson, N.A. Fleck, A.C.F. Cocks, Acta Mater. 54 (2006) 1297.
- [11] R.L. Jones, D. Mess, Surf. Coat. Technol. 86–87 (1996) 94.
- [12] C. Mercer, S. Faulhaber, A.G. Evans, R. Darolia, Acta Mater. 53 (2005) 1029.
- [13] S. Krämer, J. Yang, C.G. Levi, C.A. Johnson, J. Am. Ceram. Soc. 89 (2006) 3167.
- [14] N.P. Bansal, D. Zhu, Mater. Sci. Eng. A 459 (2007) 192.
- [15] G. Suresh, G. Seenivasan, M.V. Krishnaiah, P. Srirama Murti, J. Nucl. Mater. 249 (1997) 259.
- [16] J. Wu, X. Wei, N.P. Padture, P.G. Klemens, M. Gell, E. García, P. Miranzo, M.I. Osendi, J. Am. Ceram. Soc. 85 (2002) 3031.
- [17] Z.-G. Liu, J.-H. Ouyang, Y. Zhou, J. Alloys Compd. 472 (2009) 319.
- [18] Z.-G. Liu, J.-H. Ouyang, Y. Zhou, X.-L. Xia, Mater. Lett. 62 (2008) 4455.
- [19] H. Lehmann, D. Pitzer, G. Pracht, R. Vassen, D. Stöver, J. Am. Ceram. Soc. 86 (2003) 1338.
- [20] D. Stöver, G. Pracht, H. Lehmann, M. Dietrich, J.E. Döring, R. Vaßen, J. Therm. Spray Technol. 13 (2004) 76.
- [21] K.V.G. Kutty, S. Rajagopalan, C.K. Mathews, U.V. Varadaraju, Mater. Res. Bull. 29 (1994) 759.
- [22] S. Krämer, J. Yang, C.G. Levi, J. Am. Ceram. Soc. 91 (2008) 576.
- [23] R. Vassen, X. Cao, F. Tietz, D. Basu, D. Stöver, J. Am. Ceram. Soc. 83 (2000) 2023.
- [24] Y. Wang, F. Yang, P. Xiao, Appl. Phys. Lett. 102 (2013).
- [25] C. Wan, W. Zhang, Y. Wang, Z. Qu, A. Du, R. Wu, W. Pan, Acta Mater. 58 (2010) 6166.
- [26] B. Liu, J.Y. Wang, F.Z. Li, Y.C. Zhou, Acta Mater. 58 (2010) 4369.
- [27] J. Feng, B. Xiao, C.L. Wan, Z.X. Qu, Z.C. Huang, J.C. Chen, R. Zhou, W. Pan, Acta Mater. 59 (2011) 1742.
- [28] J. Feng, B. Xiao, R. Zhou, W. Pan, Scripta Mater. 68 (2013) 727.
- [29] D.R. Clarke, Surf. Coat. Technol. 163–164 (2003) 67.
- [30] G.A. Slack, J. Phys. Chem. Solids 34 (1973) 321.
- [31] D.G. Cahill, S.K. Watson, R.O. Pohl, Phys. Rev. B 46 (1992) 6131.
- [32] T.M. Tritt, Thermal Conductivity: Theory, Properties and Applications, Kluwer Academic/Plenum, New York, 2004.
- [33] J. Feng, B. Xiao, R. Zhou, W. Pan, Scripta Mater. 69 (2013) 401.
- [34] D.T. Morelli, J.P. Heremans, G.A. Slack, Phys. Rev. B 66 (2002) 195304.
- [35] Y. Zhang, E. Skoulios, J. Cain, V. Ozoliņš, D. Morelli, C. Wolverton, Phys. Rev. B 85 (2012) 054306.
- [36] M. Asen-Palmer, K. Bartkowski, E. Gmelin, M. Cardona, A.P. Zhernov, A.V. Inyushkin, A. Taldenkov, V.I. Ozhogin, K.M. Itoh, E.E. Haller, Phys. Rev. B 56 (1997) 9431.
- [37] T.D. Martin, Introduction to Lattice Dynamics, Cambridge University, Cambridge; New York, 1993.
- [38] L. Minervini, R.W. Grimes, K.E. Sickafus, J. Am. Ceram. Soc. 83 (2000) 1873.
- [39] G. Kresse, J. Furthmüller, Phys. Rev. B 54 (1996) 11169.
- [40] G. Kresse, J. Hafner, Phys. Rev. B 47 (1993) 558.
- [41] J.P. Perdew, K. Burke, M. Ernzerhof, Phys. Rev. Lett. 77 (1996) 3865.
- [42] A. Fujimori, F. Minami, Phys. Rev. B 30 (1984) 957.
- [43] A.I. Liechtenstein, V.I. Anisimov, J. Zaanen, Phys. Rev. B 52 (1995) R5467.
- [44] G. Kresse, D. Joubert, Phys. Rev. B 59 (1999) 1758.
- [45] S. Baroni, S. de Gironcoli, A. Dal Corso, P. Giannozzi, Rev. Modern Phys. 73 (2001) 515.
- [46] A. Togo, F. Oba, I. Tanaka, Phys. Rev. B 78 (2008) 134106.
- [47] G.A. Slack, Solid State Phys. 34 (1979) 1.
- [48] M. Roufosse, P. Klemens, Phys. Rev. B 7 (1973) 5379.
- [49] Slack GA. Solid State Phys. Academic, New York, 1979.
- [50] H.E. Hall, Solid State Physics, New York, Wiley, London, 1974.
- [51] G. Leibfried, E. Schloemann, Nachr akad wiss goettingen, Math. Phys. Klasse 4 (1954) 71.
- [52] G.A. Slack, S. Galginaitis, Phys. Rev. 133 (1964) A253.
- [53] L. Bjerg, B.B. Iversen, G.K. Madsen, Phys. Rev. B 89 (2014) 024304.
- [54] C.L. Julian, Phys. Rev. 137 (1965) A128.
- [55] A. Debernardi, M. Alouani, H. Dreyesse, Phys. Rev. B 63 (2001) 064305.
- [56] R.L. Gregory, R.W. Karl, R. Susana, L.S. Katherine, J.Z. Nestor, J. Phys. Condens. Matter 16 (2004) 8557.
- [57] M.P. van Dijk, A.J. Burggraaf, A.N. Cormack, C.R.A. Catlow, Solid State Ionics 17 (1985) 159.
- [58] A.V. Shlyakhtina, I.V. Kolbanev, A.V. Knotko, M.V. Boguslavskii, S.Y. Stefanovich, O.K. Karyagina, L.G. Shcherbakova, Inorg. Mater. 41 (2005) 854.
- [59] A.W. Sleight, Inorg. Chem. 8 (1969) 1807.
- [60] B.J. Kennedy, B.A. Hunter, C.J. Howard, J. Solid State Chem. 130 (1997) 58.
- [61] R. Shannon, Acta Crys. Sec. A 32 (1976) 751.

- [62] J.F. Nye, Physical properties of crystals, Clarendon, Oxford, 1957.
- [63] T. Kawano, H. Muta, M. Uno, Y. Ohishi, K. Kurosaki, S. Yamanaka, Mater. Res. Soc. Symp. Proc. 1514 (2013) 139.
- [64] M.P. van Dijk, K.J. de Vries, A.J. Burggraaf, Solid State Ionics 9–10 (2) (1983) 913.
- [65] K. Shimamura, T. Arima, K. Idemitsu, Y. Inagaki, Int. J. Thermophys. 28 (2007) 1074.
- [66] E.S. Toberer, A. Zevalkink, G.J. Snyder, J. Mater. Chem. 21 (2011) 15843.
- [67] W. Pan, C.L. Wan, Q. Xu, J.D. Wang, Z.X. Qu, Therm. Acta. 455 (2007) 16.
- [68] It is worth noting that Liu et al. [17] showed that Sm₂Zr₂O₇ exhibits slightly lower κ than Gd₂Zr₂O₇ at low temperature (300–700 K).
- [69] L.S. Subhash, G. Jitendra, High lattice thermal conductivity solids, Springer, New York, 2006.
- [70] K.W. Schlichting, N.P. Padture, P.G. Klemens, J. Mater. Sci. 36 (2001) 3003.
- [71] P.K. Schelling, S.R. Phillpot, R.W. Grimes, Philos. Mag. Lett. 84 (2004) 127.
- [72] Z. Qu, C. Wan, W. Pan, Acta Mater. 60 (2012) 2939.
- [73] C. Fonseca Guerra, J.-W. Handgraaf, E.J. Baerends, F.M. Bickelhaupt, J. Comput. Chem. 25 (2004) 189.